

Group Project Report
Bachelor of
Space Science and Satellite Technology

Molecular Gas in Carina Keyhole

Project by

Nguyen Thi Yen Binh, Mai Nhu Tin, Do Quoc Trong

Supervisor: Dr. Le Ngoc Tram

Mentor: Mr. Dat Thanh Hoang

Advisors: Dr. Friedrich Wyrowski and Prof. Karl Menten



University of Science and Technology of Hanoi
Hanoi, Vietnam
2022

Contents

1	Introduction	3
2	Theoretical background and state of current research	4
2.1	Molecular cloud	4
2.2	Radiative Transfer	4
2.3	Photodissociation Region	4
3	Scientific methods and materials	5
3.1	Observational Data	5
3.1.1	APEX observations	5
3.1.2	SOFIA/GREAT observations	5
3.1.3	Herschel observations	5
3.2	LTE and non-LTE conditions	5
3.2.1	LTE method	5
3.2.2	Dust continuum	8
3.2.3	Non-LTE method using Radex	8
3.3	PDR Toolbox	8
3.4	Photo-Dissociation Rate	9
3.4.1	Shielding effect	9
3.4.2	Time needed to fully dissociate CO clouds	9
4	Results(3 pages)	11
4.1	Integrated Intensity Maps	11
4.2	Spectral Lines	11
4.3	Physical Properties	12
4.3.1	Observational constraints and Dust Continuum constraints	12
4.3.2	Gas Density and Temperature in non-LTE constraint	13
4.3.3	Radiation Strength	13
4.3.4	Photo-Dissociation of CO	14
5	Discussion	15
5.1	Motion of Molecular Gas	15
5.2	Shielding function	15
5.3	Number of CO molecules	15
6	Scientific Conclusions	16
7	Management of the project	17
8	References	19
9	Appendix	21

List of Figures

1	Integrated intensity maps of $^{12}\text{CO}(2-1)$	11
2	Physical constraint using RADEX of Region 1-5	22
3	Overlay plots show the observed intensity ratios in the G_0 and n_H grids of the PDR Toolbox. The shaded area represents the observational error.	23
4	Shielding function by gas and ^{12}CO at $T_{ex} = 20K$ and $T_{ex} = 5K$	23
5	Representative spectra of $^{12}\text{CO}(2-1)$, $^{13}\text{CO}(3-2)$, $^{13}\text{CO}(2-1)$, $C^{18}\text{O}(2-1)$, $[\text{C I}] 609\mu\text{m}$, $^{12}\text{CO}(3-2)$, $^{12}\text{CO}(8-7)$, $[\text{N II}] 205\mu\text{m}$, $[\text{O I}] 63\mu\text{m}$ and 21 cm H towards the 7 regions.	26
6	The WK2006 model for the ratio of the $[\text{C I}] 609\mu\text{m}$ and $^{12}\text{CO}(3-2)$ (top left), $[\text{C II}] 158\mu\text{m}/^{12}\text{CO}(3-2)$ (top right) and $[\text{C II}] 158\mu\text{m}/[\text{C I}] 609\mu\text{m}$ (bottom), computed as a function of hydrogen nucleus density n_H and FUV field G_0	27
7	The top panel shows the fitted dust temperature T_d map, and the bottom panel shows the corresponding column density N_{H_2} map. Each map is smoothed to the 35.2 beam size of the Herschel 500 m observations	28

1 Introduction

The feedback from the massive star or cluster regulates the physical and chemical of the parental molecular cloud. The radiative feedback could directly dissociate the molecules. It is well-known that the strong radiation field can dissociate molecular hydrogen and ionize the atomic hydrogen, creating a HII region around the source. The edge of this HII region defines the photo-dissociation (PDR) region, in which molecules with lower dissociation and ionization potential could be further dissociated and ionized.

Trumpler 16 (Tr 16), including η -Carina, is one of the most massive star clusters. The radiation field from the O and B members of Tr 16 are demonstrated to be more than enough to externally excite the nearby cloud without needing the embedded sources (Oberst et al. 2011, [11]). Furthermore, the expanding wind of 20 km s^{-1} supplied by the central source can also sculpt and alter the nearby cloud properties. Thus, this region is an ideal target to study the interaction between the feedback and the surrounding molecular cloud. Cox et al. (2015) reported the existence of several CO clumps in the cloud nearby η -Carina, known as a Keyhole. Two fundamental questions remained (i) how this nearby cloud can resist the energetic feedback from the cluster, and (ii) how the molecular gas can survive in the photon-dominated region, which we expect CO being photo-dissociated.

Recently, the role of the magnetic field has been considered in the formation and evolution of the parental cloud due to the tremendous polarimetric observations. For instance, the orientation of the ambient magnetic field could affect the shape of the molecular clouds under the impact. Skafididis et al. 2021 [18] showed that the magnetic field plays an important role where HI-H2 transition occurs, and the atomic gas could accumulate along the field lines to form the molecular gas. However, Seo et al. 2021 [17] concluded that the magnetic field is not strong enough to go against the η -Carina feedback in the case of the Keyhole. Thus, we could rule out the case that the CO is newly formed inside the Keyhole.

The self- and mutual-shielding significantly affect the photo-dissociation rate of CO (Visser & van Dishoeck et al. 2009, [22]). CO could survive when the visual extinction is about 6. Thus, shielding is a reasonable interpretation to explain the existence of CO clumps that we expect to reveal in this project.

In this work, we revisit this region of Keyhole by using the new observations of CO(2-1) and CI lines with APEX telescope to characterize the physical properties of the molecular clumps in assumptions of local thermal equilibrium (LTE) and non-local thermal equilibrium (non-LTE) conditions and combine them with the dust continuum to quantify the photo-dissociation process at each clump.

2 Theoretical background and state of current research

2.1 Molecular cloud

A molecular cloud is an interstellar gas condensation in which the atoms are bonded together as molecules rather than as free atoms or charged particles. The state of interstellar gas is largely determined by its density and temperature, and molecular clouds are the coldest, densest phase of the interstellar medium. Molecules in the interstellar medium are identified by characteristic emission (or absorption) lines in their spectra. Molecules can rotate around or vibrate along the interatomic axes defined by the chemical bonds. It is the transition from one rotational or vibrational state to another of individual molecules that gives rise to the spectral lines of a molecular gas. The spectral lines from each molecule are unique. The rotational and vibrational transitions occur primarily in the infrared and radio portions of the electromagnetic spectrum thus molecular clouds are detected primarily by infrared and radio telescopes.

2.2 Radiative Transfer

The radiative transfer equation (Spitzer 1978 [19]; Draine 2011 [2]) is written in term of specific intensity I_ν because I_ν remains constant along the line of sight if there is no interaction in the propagation of light:

$$\frac{dI_\nu}{ds} = j_\nu - \alpha_\nu I_\nu \quad (1)$$

where α_ν is the absorption coefficient in $[\text{cm}^{-1}]$, j_ν is the emission coefficient in $[\text{erg cm}^{-3} \text{s}^{-1} \text{Hz}^{-1} \text{sr}^{-1}]$.

By defining the optical depth as $d\tau_\nu \equiv \alpha_\nu ds$, we can rewrite this equation in the following form:

$$\frac{dI_\nu}{d\tau_\nu} = S_\nu - I_\nu \quad (2)$$

where the source function S_ν is the ratio of emission to absorption coefficient.

The formal solution for this equation can be written as:

$$I_\nu(\tau_\nu) = I_\nu(0)e^{-\tau_\nu} + \int_0^{\tau_\nu} e^{-(\tau_\nu)-\tau'_\nu} S_\nu(\tau'_\nu) d\tau'_\nu \quad (3)$$

2.3 Photodissociation Region

Photodissociation regions (PDRs) are created by the penetration of far-UV (FUV) radiation into molecular clouds. The FUV radiation dissociates the molecules and heats the gas and dust. A warm HII region is thus created in the boundary of a molecular cloud, and the chemistry and thermal balance of the region are determined by the radiation field. The FUV radiation also ionizes several species with ionization energies lower than 13.6 eV. The CO is photodissociated and the resulting C is singly ionized throughout the PDR by the FUV radiation. O/B stars near or inside molecular clouds produce PDRs. For this reason PDRs are often observed in association with HII regions as the interface between the ionized and the molecular gas (V. Escalante, Sternberg & Dalgarno 1991, [3]).

3 Scientific methods and materials

3.1 Observational Data

3.1.1 APEX observations

We use the new observations of CO lines from the FLASH receiver on Atacama Pathfinder EXperiment (APEX) telescope.

3.1.2 SOFIA/GREAT observations

We used the archival data measured by the GREAT instrument onboard the Stratospheric Observatory for Infrared Astronomy (SOFIA).

3.1.3 Herschel observations

We combine the archival data of Herschel/PACs at 70 and 160 μm , and Herschel/SPIRE at 250, 350, and 500 μm to build the spectral energy distribution (e.g., flux vs. wavelengths). The procedure is as below

- We smooth all the data to the lowest resolution of 35.2''-FWHM (full width at half maximum) of Herschel/SPIRE 500 μm , using a Gaussian kernel,
- We re-grid all the smoothed data to the maps with a common pixel size of 3.2'', equivalent to the smallest pixel size of the Herschel/PACs data at 70 μm .

3.2 LTE and non-LTE conditions

3.2.1 LTE method

Our interest is in spectroscopy, so we shall deduce α_ν and j_ν in terms of Einstein coefficients. We define the emission coefficient j_ν based on the process of deexcitation:

$$j_\nu = \frac{h\nu}{4\pi} n_u A_{ul} \phi_\nu \quad (4)$$

The 4π term is due to the assumption that the emission is isotropic, the ϕ_ν is the line profile is the function taking care of the line shape, which must be hold $\int \phi(\nu) d\nu = 1$.

For the absorption coefficient, we find in a similar way. It seems that the stimulated process should add into the emission coefficient, however in practice the spontaneous excitation and stimulated deexcitation always occur together. As the result, we will treat this term as a "negative value" of the extinction process:

$$\alpha_\nu = \frac{h\nu}{4\pi} (n_l B_{lu} - n_u B_{ul}) \phi_\nu \quad (5)$$

When the matter is in equilibrium with radiation in thermodynamic equilibrium, the level populations must reach the Boltzmann distribution, the Einstein relations can be derived as:

$$g_l B_{lu} = g_u B_{ul} \quad (6)$$

and,

$$A_{ul} = \frac{2h\nu^3}{c^2} B_{ul} \quad (7)$$

With expression of j_ν and α_ν , the source function can be derived in terms of Einstein coefficients:

$$S_\nu = \frac{A_{ul}}{B_{ul}} \frac{1}{\frac{n_l}{g_l} \frac{g_u}{n_u} - 1} \quad (8)$$

We can define an excitation temperature to characterize the ratio of n_l/n_u :

$$\frac{n_u}{n_l} = \frac{g_u}{g_l} e^{-\frac{h\nu}{kT_{ex}}} \quad (9)$$

By this definition, the source function becomes

$$S_\nu = B_\nu(T_{ex}) \quad (10)$$

If the line is optically thin ($\tau_\nu \ll 1$), we can simply ignore the optical depth and write the radiative transfer equation as:

$$dI_\nu = j_\nu ds = \frac{h\nu}{4\pi} A_{ul} n_u \phi_\nu ds \quad (11)$$

Define the so-called column density in a level as $N_u = \int n_u ds$, we can integrate both sides of this equation:

$$I_\nu = \frac{h\nu}{4\pi} A_{ul} N_u \phi_\nu \quad (12)$$

Continued by integration of both sides over the frequency ν field, with the condition of line profile function that $\int \phi_\nu d\nu = 1$. The column density of the gas in the excited state u can be expressed as:

$$N_u = \frac{4\pi}{h\nu A_{ul}} \int I_\nu d\nu = \frac{8\pi k_B \nu^2}{hc^3 A_{ul}} \int T_{mb} dv \quad (13)$$

The total column density can be related to N_u assuming detailed balance at a constant temperature defined by the excitation temperature T_{ex} as:

$$\frac{N_{tot}}{N_u} = \frac{Q_{rot}}{g_u} \times \exp\left(-\frac{E_u}{k_B T_{ex}}\right) \quad (14)$$

where the rotational partition function Q_{rot} is introduced as a quantity to represent a statistical sum over all rotational energy levels in the molecule.

$$Q_{rot} = \sum_{j=0}^{\infty} (2J+1) \times \exp\left(-\frac{E_j}{k_B T}\right) \quad (15)$$

Combine all the terms above, the equation for the total column density of the gas can be expressed as following:

$$N_{tot}^{thin} = \frac{8\pi k_B \nu^2}{hc^3 A_{ul}} \frac{Q_{rot}}{g_u} \exp\left(-\frac{E_u}{k_B T_{ex}}\right) \int T_{mb} dv \quad (16)$$

If the line is not optical thin line, a column density calculated having the contribution from optical depth value by the following relation (Mangum 2017 [8]):

$$N_{tot} = N_{tot}^{thin} \frac{\tau}{1 - e^{-\tau}} \quad (17)$$

The factor $\frac{\tau}{1 - e^{-\tau}}$ is defined as the *optical depth correction factor* (Goldsmith & Langer 1999 [4]).

Optical depth: With the assumption of constant excitation temperature for ^{12}CO and ^{13}CO (Roueff et al. 2020 [15]). We can constraint the value of optical depth for $^{13}CO(2-1)$ using the another assumption that $^{12}CO(2-1)$ is an optically thick line with the value of $\tau_\nu^{12} \rightarrow \infty$. We can consider a rotational transition at frequency ν assuming that the beam filling factor equal one and $T_{bg} = 2.73$ is the Cosmic Microwave Background (CMB), the Rayleigh Jean equivalent temperature in LTE for $^{12}CO(2-1)$ is expressed as:

$$T_R^{12} = J_\nu^{12}(T_{ex}) - J_\nu^{12}(T_{bg}) \quad (18)$$

where $J_\nu(T) = \frac{h\nu}{e^{h\nu/T} - 1}$.

Then, we can constrain each region's value for T_{ex} . Then put the value of T_{ex} back into the equation for LTE to find the optical depth of $^{13}CO(2-1)$ as:

$$\tau_\nu^{13} = -\ln\left(1 - \frac{T_R^{13}}{J_\nu^{13}(T_{ex}) - J_\nu^{13}(T_{bg})}\right) \quad (19)$$

Column density: Having the value for optical depth of $^{13}CO(2-1)$, we can use the equation for N_{tot} to estimate the column density of ^{13}CO . Using the abundance of ^{12}CO to ^{13}CO of 65 based on the average local ISM $^{12}C/^{13}C$ ratio of 68 ± 15 found by Milam et al. (2005), we can deduce N_{CO} , the column density of ^{12}CO , given in 10^{17} cm^{-2} . Then, we can estimate the value of the total column density of H_2 , $N(H_2) = 10^4 N(CO)$ given in 10^{21} cm^{-2} . Also, the A_v , visual extinction can be derived from ratio $\frac{N(H_2)}{A_v} = 9.4 \times 10^{20} \text{ cm}^{-2} \text{ mag}^{-1}$ (Pineda et al. 2008 [12]).

Mass of the gas: We will finally derive the mass of the gas from the measurement of total column density N_{H_2} by the following expression:

$$M_{H_2} = \mu_{H_2} m_H A N(H_2) \quad (20)$$

where $A = \pi ab$ is the area of 7 elliptical regions constraining in our molecular cloud in which a, b is the width and height of the area respectively, $m_H = 1.66 \times 10^{-24} \text{ g}$ is the mass of a proton. Since the molecular cloud mostly contains H_2 , but they also have a small amount of other heavier atom (e.g., He , CO), the mean molecular weight of the hydrogen gas in the cloud $\mu_{H_2} = 2.8$ used for correction.

Density of the gas: We can define density of gas in a similar way to the mass, in which we consider the region is spherical with equivalent radius $R_{equi} = \sqrt{ab}$ (cm):

$$n(H_2) = \frac{AN(H_2)}{V} \quad (21)$$

where $V = \frac{4}{3}\pi R_{equi}^3$ (cm^{-3}).

3.2.2 Dust continuum

In order to constrain dust column densities and temperatures, the spectral energy distribution (SED) for each pixel can be fitted using Herschel data at 70, 160, 250, 350, 500 μm to a modified blackbody function (Karoly 2020 [5]):

$$S_\nu = B_\nu(T_d)(1 - e^{-\tau_\nu}) \quad (22)$$

where $B_\nu(T_d) = \frac{2h\nu^3}{c^2} \frac{1}{e^{h\nu/k_B T_d}}$ and $\tau_\nu = \mu_{H_2} m_H \kappa_0 \left(\frac{\nu}{\nu_0}\right)^\beta N_{H_2}$. In this equation, we choose the emissivity spectral index of the dust $\beta = 2$ and we assume that $\kappa_0 = 0.1 \text{ cm}^2\text{g}^{-1}$ and $\nu_0 = 10^{12} \text{ Hz}$ (Beckwith et al. 1990). So there are two free parameters to constrain

3.2.3 Non-LTE method using Radex

In the LTE method, the results obtained from many strong assumptions, for instance, the excitation temperature of ^{12}CO and ^{13}CO are the same. To address this issue, we used the non-LTE radiative transfer RADEX code (van der Tak et al. 2007 [20]), a numerical method for solving the radiative transfer equation in an isothermal and homogeneous based on the escape probability. The program made use of the input format for spectroscopic and collisional data provided by the LAMDA database (Schöier et al. 2005 [16]) to constrain the physical conditions such as the kinetic temperature (T_{kin}), the density of collision partners (n_{H_2}) and the column density (N_{CO}).

Escape probability: In order to simplify the calculation, RADEX introduced a geometrically averaged escape probability, the probability that a photon will escape the medium from where it was created, which depends only on the optical depth τ and related to the intensity within the medium. In three available geometries, we choose the expanding spherical shell with the escape probability expressed by the following equation (Mihalas 1978 [10]):

$$\beta_{LVG} = \frac{1 - e^{-\tau}}{\tau} \quad (23)$$

The result from LTE method provide that the column density of CO varied around $10^{16} - 10^{18}$. In 7 inputs from RADEX, we have three unknown parameters: kinetic temperature T_{kin} , density of collision partner $n(H_2)$ and column density of gas $N(CO)$ to constrain. We fixed the value of $N(CO)$ of 10^{16} , 10^{17} , 10^{18} and make a grid of models from T_{kin} and $n(H_2)$. We, then, estimated the .After that we can run RADEX for each pixel to make a grid of intensity of line $CO(2-1)/CO(3-2)$, $CO(3-2)/CO(8-7)$ and $CO(2-1)/CO(8-7)$ and draw the contour line of observed values from the spectral data on the grid to constrain the value of T_{kin} and $n(H_2)$.

3.3 PDR Toolbox

To assess the physical conditions in photodissociation regions include the far UV flux in Habing units (Habing 1968, 1 Habing = $G_0 = 1.63 \times 10^{-3} \text{ erg cm}^{-2} \text{ s}^{-1}$) and H nucleus density ($n_H, \text{ cm}^{-3}$) from observations, we utilized the PDR Toolbox (Kaufman et al. 2006[6]; Pound and Wolfire 2008, 2011[13][14]), a Python package that leverages state-of-the-art PDR models.

We used both techniques that available in PDR toolbox that are The Levenberg-Marquardt least squares fit (LSQ) technique determines best G_0 and n_H by minimizing the χ^2 of the observed intensity ratios vs the projected model intensity ratios, weighted by the inverse square of the observational errors. And the Markov Chain Monte Carlo (MCMC) method is used to calculate the posterior probability density functions (PDFs) of G_0 and n_H . In this study, we publish the values generated by the LSQ approach since the predicted G_0 and n_H from the two methods are consistent.

We have extracted the value of n_H and G_0 from the observations line intensities of $^{12}\text{CO}(3-2)$, $609\ \mu\text{m}$ [C I] and $158\ \mu\text{m}$ [C II] for the region 1. The integrated intensities of $^{12}\text{CO}(3-2)$ and $609\ \mu\text{m}$ [C I] were estimated from the whole spectra from $-50\ \text{km/s}$ to $20\ \text{km/s}$ velocity range. The $158\ \mu\text{m}$ [C II] intensity was taken from The Long Wavelength Spectrometer (LWS; Clegg et al. 1996[1]) aboard the Infrared Satellite Observatory (ISO; Kessler et al. 1996[7]) was used to obtain full bandwidth ($43\text{--}197\ \mu\text{m}$) spectra of the Carina Nebula over four days—1996 July 23 and 24 and August 1 and 4—as part of a guaranteed time observation (GTO) by T. Onaka. For more details see Oberst et al. 2011, [11].

3.4 Photo-Dissociation Rate

3.4.1 Shielding effect

Since UV radiation creates a photo-dissociation region and strongly promotes the dissociation of CO molecules, gas molecules and dust inside the clouds can shield around the CO molecules and then allow them to survive energetic radiation, it is called the shielding effect.

Self-shielding, shielding by H, H_2 and the other CO isotopologues, and continuum shielding by dust all reduce the photo-dissociation rates inside a cloud or other environment relative to the unshielded rates (van Dishoeck et al. 2006 [21]). For a given combination of column densities (N) and visual extinction (A_V), the shielded photo-dissociation rate for isotopologue i is:

$$k_i = \chi k_{0,i} \Theta_i \exp\{(-\gamma A_V)\} \quad (24)$$

with χ a scaling factor for the UV intensity and $k_{0,i}$ the unattenuated rate in a given radiation field. The shielding function Θ_i accounts for self-shielding and shielding by H, H_2 and the other CO isotopologues. The dust extinction term, $\exp(-\gamma A_V)$ shows the effect of dust shielding on the photo-dissociation rate. The exponential function pointed out that dust shielding is a strong influential component, while the linear function of self- and mutual-shielding of gas and isotopologues is the less influential factor.

3.4.2 Time needed to fully dissociate CO clouds

To answer the initial question, the idea is to compare the time that a CO cloud needed to be fully dissociated by radiation of $\eta - \text{Carina}$ to the age of this star.

Since the photo-dissociation rate is calculated, the time needed for a CO cloud to be fully dissociated can be inferred. Assuming the regions are circles or ellipses in a plane (perpendicular to the line of sight), it is possible to determine their areas.

$$A = \pi a \times b \quad (25)$$

where a is the semi-major axis and b is the semi-minor axis when the region is an ellipse, $a = b$ when the region is a circle.

The number of CO molecules in each region at the time the observation is made can be calculated as:

$$n_{current}^{CO} = N(CO) \times A \quad (26)$$

The time needed to completely dissociate a CO cloud is:

$$t_{PD} = n_{current}^{CO} \times k_{CO} \quad (27)$$

Hence, the shielding effect is a good candidate to strictly prove the presence of CO cloud as t_{PD} is larger than the age of $\eta - Carina$.

4 Results(3 pages)

4.1 Integrated Intensity Maps

The zeroth moment or integrated intensity can be expressed as the integral of the intensity over the velocity on the spectral axis:

$$M_0 = \int I_v dv \quad (28)$$

The Figure 1 shows the zeroth-moment map of the $^{12}\text{CO}(2-1)$ line. All pixels with the peak value of $T_{mb} < 3\sigma$ are removed from the map. Remaining pixels can be considered as the real signal from $^{12}\text{CO}(2-1)$ line. We marked out 7 regions that showing very strong signal of $^{12}\text{CO}(2-1)$, another regions are not circled cause it does not belong to the Keyhole (our main study object) or the pixel value is not high enough.

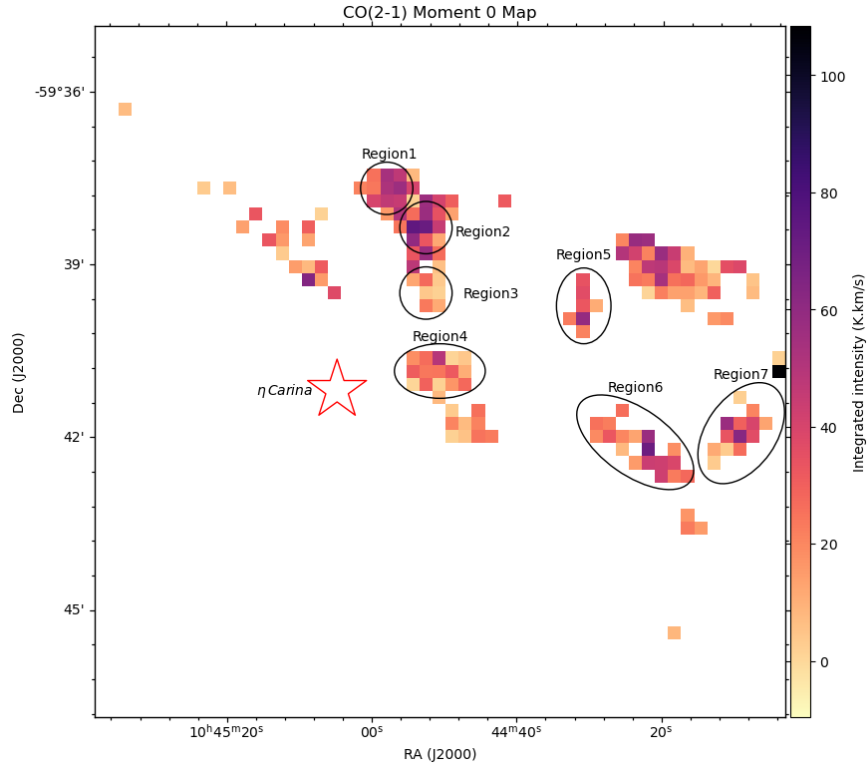


Figure 1: Integrated intensity maps of $^{12}\text{CO}(2-1)$

4.2 Spectral Lines

Figure 5 shows the representative spectra of $^{12}\text{CO}(2-1)$, $^{13}\text{CO}(3-2)$, $^{13}\text{CO}(2-1)$, $C^{18}\text{O}(2-1)$, $[\text{C I}] 609\mu\text{m}$, $^{12}\text{CO}(3-2)$, $^{12}\text{CO}(8-7)$, $[\text{N II}] 205\mu\text{m}$, $[\text{O I}] 63\mu\text{m}$ and 21 cm H towards the 7 regions. We fitted these spectra with Gaussian function. For each line, our confident signal is selected between $\mu + 3$ and $\mu - 3\sigma$, which accounts for 99.7% of the signal. We could see there are some regions (2,4,6) that can be fitted with two Gaussian, means

that there are two distinct clumps of gas in our spectra. The similarity in peak position and profile of all tracers for position ensures that we are tracing the same gas. We can see that the ^{13}CO spectral profile follows that of ^{12}CO , suggesting no self absorption in ^{12}CO from any cold foreground.

4.3 Physical Properties

In our study, we try to determine some physical conditions of each region in molecular gas, such as column density N_{CO} , kinetic temperature T_{kin} , the mass of the gas M_{gas} and density of the gas n_{gas} . We will estimate the physical conditions under the assumption of local thermodynamic equilibrium (LTE) and then compare them with the results adopted for the dust continuum. Since the LTE method is based on many strong assumptions, we try to get more general results of physical conditions by making use of RADEX.

4.3.1 Observational constraints and Dust Continuum constraints

region	$T_{\text{mb}}^{\text{max}}$ (K)	\bar{v}_{LST} (km s $^{-1}$)	σ_v (km s $^{-1}$)
#1	10.66	-17.2	1.04
#2	7.42	-31.93	0.93
#3	5.82	-31.92	0.77
#4	2.41	-7.81	1.81
#5	3.63	-24.84	1.13
#6	1.53	-6.37	0.98
#7	3.52	-30.98	0.88

Table 1: Observational values of CO(2-1) from spectral data. The first column is peak main beam temperature $T_{\text{mb}} = T_A/\eta$ where T_A is the antenna temperature and main beam efficiency $\eta = 0.82$, the local standard of rest velocity \bar{v}_{LST} , and standard deviation σ_v obtained directly from spectral data.

In order to constrain dust column densities and temperatures, the spectral energy distribution (SED) for each pixel can be fitted using Herschel data at 70, 160, 250, 350, 500 μm to a modified blackbody function (Karoly 2020 [5]):

$$S_\nu = B_\nu(T_d)(1 - e^{-\tau_\nu}) \quad (29)$$

where $B_\nu(T_d) = \frac{2h\nu^3}{c^2} \frac{1}{e^{h\nu/k_B T_d}}$ and $\tau_\nu = \mu_{\text{H}_2} m_H \kappa_0 \left(\frac{\nu}{\nu_0}\right)^\beta N_{\text{H}_2}$. In this equation, we choose the emissivity spectral index of the dust $\beta = 2$ and we assume that $\kappa_0 = 0.1 \text{ cm}^2\text{g}^{-1}$ and $\nu_0 = 10^{12} \text{ Hz}$ (Beckwith et al. 1990). The temperature and column density maps obtained from SED fitting procedure are shown in figure 7.

region	$N(^{13}\text{CO})$ (10^{15} cm^{-2})	$N(\text{CO})$ (10^{17} cm^{-2})	T_{ex} (K)	$N(\text{H}_2)^{\text{CO}}$ (10^{21} cm^{-2})	$N(\text{H}_2)^{\text{dust}}$ (10^{21} cm^{-2})	A_V	$M_{\text{gas}}^{\text{CO}}$ (M_{\odot})	$M_{\text{gas}}^{\text{dust}}$ (M_{\odot})	$n(\text{H}_2)^{\text{CO}}$ (10^3 cm^{-3})	$n(\text{H}_2)^{\text{dust}}$ cm^{-3}	T_{dust} (K)
#1	6.09	3.96	17.37	3.96	2.21	4.97	4.07	2.27	5.93	2.81	39.39
#2	2.11	1.37	13.89	1.37	2.71	1.65	1.43	2.83	1.96	3.41	38.35
#3	0.80	0.52	12.10	0.52	1.95	0.62	0.59	2.21	0.71	2.36	40.06
#4	1.45	0.94	7.90	0.94	1.58	1.15	4.71	7.87	0.62	0.91	38.10
#5	1.96	1.28	9.62	1.28	1.54	1.57	6.36	7.66	0.63	0.66	34.89
#6	1.60	1.04	6.60	1.04	1.24	1.30	6.30	7.55	0.59	0.60	32.05
#7	0.97	0.63	9.37	0.63	1.36	0.76	4.06	8.72	0.53	1.01	30.62

Table 2: Observational constraints. The value of $N(^{13}\text{CO})$ is estimated by equation 17 using the value of optical depth calculated by equation 19, $N(\text{CO})$ are given by the abundance of $^{12}\text{CO}/^{13}\text{CO} = 65$. The excitation temperature T_{ex} , total column density $N(\text{H}_2)^{\text{CO}}$ from CO, the visual extinction A_V , the mass of gas to mass of sun from CO $M_{\text{gas}}^{\text{CO}}$, the gas density $n(\text{H}_2)^{\text{CO}}$ from CO are calculated under LTE condition described in section 3.2.1. While the total column density $N(\text{H}_2)^{\text{dust}}$, gas density $n(\text{H}_2)^{\text{dust}}$ and dust temperature T_{dust} of each region are estimated on average under SED condition.

4.3.2 Gas Density and Temperature in non-LTE constraint

For non-LTE method, $N(\text{CO})$ are fix parameter, $n(\text{H}_2)$ range from 10 to 10^{13} , T_{kin} range from 10 to 500 K. The results obtained are shown in figure 2. We argued that 3 CO lines traced the same parameter, so the point where three lines intersect is the value constrained. However from the figure 2, it can be seen that while line ratio of CO(3-2)/CO(8-7) and CO(2-1)/CO(8-7) are good tracers, line ratio of CO(2-1)/CO(3-2) is bad. Therefore, we can constraint the gas density and temperature of region #1 to region #5 in the range between two lines of CO(8-7). Region #6 and #7 can not be constrained because the we do not have data of intensity of CO(8-7) in those two regions.

region	T_{kin} (K)	n_{gas} (cm^{-3})	$N(\text{CO})$ (cm^{-2})
#1	100 - 110	$10^4 - 10^5$	$10^{16} - 10^{17}$
#2	60 - 70	$10^4 - 10^5$	$10^{16} - 10^{17}$
#3	30	$10^3 - 10^4$	$10^{16} - 10^{17}$
#4	60 - 80	$10^4 - 10^5$	$10^{16} - 10^{17}$
#5	60 - 80	$10^4 - 10^5$	$10^{16} - 10^{17}$
#6	-	-	-
#7	-	-	-

Table 3: non-LTE constraints

4.3.3 Radiation Strength

With the model, the density, n_H , is well constrained by the line intensities ratio between $609 \mu\text{m}$ [C I] and $^{12}\text{CO}(3-2)$. On the other hand, the ratio $158 \mu\text{m}$ [C II]/ $609 \mu\text{m}$ [C I] and $158 \mu\text{m}$ [C II]/ $^{12}\text{CO}(3-2)$ are helpful for determining the field G_0 (Figure 6). Our PDR model results are shown in Figure 3, where three contours cross each other, we found that

region	A_V	k (Molecule $\times s^{-1}$)	$n_{current}^{CO}$ (Molecules)	$\Delta n_{etacar}^{CO} (*)$ (Molecules)	t_{PD} (<i>Million</i> years)
#1	4.97	2.016765×10^{-20}	1.739177×10^{54}	0	2.734525×10^{60}
#2	1.65	3.994341×10^{-15}	6.116737×10^{53}	0	4.855881×10^{54}
#3	0.62	5.877838×10^{-13}	2.519682×10^{53}	55	1.359319×10^{52}
#4	1.15	6.925073×10^{-14}	2.418092×10^{54}	6	1.107240×10^{54}
#5	1.57	1.572314×10^{-14}	2.729571×10^{54}	1	5.504887×10^{54}
#6	1.30	4.078171×10^{-14}	4.811481×10^{54}	3	3.741164×10^{54}
#7	0.76	3.585826×10^{-13}	2.594857×10^{54}	33	2.294655×10^{53}

Table 4: Photo-Dissociation information of each region. The first column is the visual extinction. The second column shows the shielded photo-dissociation rate of CO. The third column is the number of CO molecules inside each cloud when the observation was made. The number of fully dissociated molecules is shown in the fourth column. The last column is the time needed to completely dissociate the whole CO cloud. (*) These values were rounded to the closest integer numbers.

the radiation field is just about 7.3 Habing, more than 7 times compared to local interstellar radiation field, which is not consistent with the distance very close to a strong UV radiation source η Carina, and very dense hydrogen nucleus $151 \times 10^3/cm^3$.

4.3.4 Photo-Dissociation of CO

The dependence of the shielding function Θ on the gas column density is shown in Figure 4 (Data of the shielding function from Visser, van Dishoeck & Black 2009[22]¹). At low column density, the shielding value is approximately high, corresponding to this is the weak-shielded case. In contrast, the effect of shielding is remarkable in the case of high column density. The shielding function Θ_i also is affected by the excitation temperature, the shielding effect is stronger in the case of higher temperature.

From equation (6), $\chi = 4.28 \pm 0.25$ (Draine unit) and $k_0 = 2.6 \times 10^{-10}s^{-1}$ for ^{12}CO (Visser, van Dishoeck Black 2009 [22]). The extinction coefficient γ is 3.53 for ^{12}CO (Visser, van Dishoeck Black 2009 [22]).

Using the method mentioned in section 3.3, the shielded photo-dissociation rates of CO in 7 regions resulted in the range of $10^{-13}s^{-1}$ to $10^{-20}s^{-1}$ (see Table 4). Since the photo-dissociation rate is calculated, the time needed for a CO cloud to be fully dissociated can be inferred. In this project's considered regions, it takes at least 10^{54} million years to completely dissociate a CO region. These results are significantly higher than the age of $\eta - Carina$ which is 3 million years (Andrea Mehner, Kris Davidson, Gary J. Ferland, and Roberta M. Humphreys 2010 [9]), hence it interprets the dense presence of CO clouds in the proximity of $\eta - Carina$.

¹https://home.strw.leidenuniv.nl/~ewine/photo/CO_photodissociation.html

5 Discussion

5.1 Motion of Molecular Gas

The spectral lines belong to 7 regions show strong line splitting. The radial velocity of ^{12}CO line in region 1 is about -17 km/s very close to the VLSR of η Carina about -20 km/s. Furthermore, the velocity components of molecular gas belong to another regions are far away this value. There is a very strong emission line of CO at -32 km/s in region 2 and region 3. Although in the region 2 there are two peaks and the remaining peak is about -20 km/s that is the same with η Carina but this one does not dominant the strong emission of CO in this region. For region 4, the spectra indicate that there are two clumps of gas moving with velocity around -8 km/s and 9 km/s; -7 km/s and -1 km/s in region 6. The clumps in region 5 and 7 move with velocity around -25 km/s and -31 km/s respectively. From these, we could come up with the idea that these 7 regions are not belong to the molecular gas around η Carina, so that we could understand why the radiation field is very low

5.2 Shielding function

The data of shielding function from Visser, van Dishoeck Black 2009 [22] contains certain conditions of temperature (5K, 20K, 100K, 500K), but our excitation temperatures of considered regions do not exactly match these conditions. Hence, we approximately use the shielding function at the temperature which is closest to T_{ex} of each region (e.g regions 1 and 2 are close to 20K, and other regions are close to 5K).

A better result can be obtained by using the interpolating method. From that, we could find out a shielding function depending on temperature, based on the given data. Hence the more precise shielding function can be accessed and then reveal a more accurate photo-dissociation rate. However, it is expected to not change the order of magnitude by more than 2, thus the general picture of photo-dissociation of CO is held in our current method.

5.3 Number of CO molecules

To calculate the number of CO molecules in each cloud, we assumed the regions are circles and ellipses in a plane perpendicular to the line of sight (section 3.4.2) because the column densities inferred from the LTE condition have the unit of *molecules/cm²* which is the number of molecules on a plane perpendicular to the line of sight. This is a regular disadvantage in Astronomy because telescopes just can observe celestial objects as 2D images.

We can instead use the 3D column densities to infer the result, but we cannot check the 3D density due to the limitations of current technology. The volume of the cloud which is roughly assumed to be spherical in section 3.2.1 will give rise to a less accurate result.

6 Scientific Conclusions

The presence of CO molecules in the proximity of a highly-emitted UV radiation source such as $\eta - Carina$ must be pointless if they exist without any support from other physical phenomena. This project determined the photo-dissociation rate of CO molecules in each region and pointed out that the time needed to fully dissociate remaining CO clouds is larger than the age of $\eta - Carina$ which interpreted the presence of CO regions that we observed previously.

Additionally, this result reinforces the conclusion of Visser, van Dishoeck & Black 2009[22] about the influence of the shielding effect on the photo-dissociation rate of molecules in the interstellar medium.

In the future step of this project, we will continue to analyze the motion of molecular gas in these clouds, and the impact of the feedback on our clumps.

7 Management of the project

This section is an assessment of what has been done with what has been planned.

We did follow the plan as much as we could, however, there are some unexpected issues during the project which are shown clearly in Table 2. Problems mainly occurred in the middle phases because of lacking experience in working with the Ubuntu system and misunderstanding of some new definitions in this topic.

On the good side, the deadline of the schedule in each phase was kept strictly on time, hence there were no significant delays. The members were very self-disciplined in their work.

Plan	Done	Cause of the difference
Basic lectures in Spectroscopy and Literature review	Finished lectures and review	None
We will analyze a set of data of $^{12}\text{CO}(2-1)$, $^{12}\text{CO}(8-7)$, $^{13}\text{CO}(2-1)$, $^{13}\text{CO}(3-2)$, $^{12}\text{C}^{18}\text{O}(2-1)$, CI, HI, OI lines	We analyzed planned data and found the locations of 7 regions with almost their characteristics	Some lines of data could not be fitted by the Gaussian fitting. But the results were done by using another method.
<ul style="list-style-type: none"> • Constrain column density, optical depth and temperature of H_2 and CO from Data in LTE and non-LTE conditions from results of the previous step • We then use Astrochem platform to determine the main reactions of CO in considered clouds 	<ul style="list-style-type: none"> • We found the physical parameters in the LTE condition and the non-LTE condition • We continued to calculate the same parameters with data from dust continuum spectrum • We did not work with Astrochem platform 	<ul style="list-style-type: none"> • Dust continuum is an important spectrum that can be used to constrain physical properties such as gas column density and temperature besides spectral lines of molecules, atoms and ions. Hence, this spectrum will be used as a reference for double-checking the analysis of the spectral lines • We could not access the Astrochem platform because of a technical problem with the Ubuntu system
Analyze Photodissociation of CO and infer the physical interpretation of results	We analyzed photodissociation of CO and found the physical background behind the existence of CO.	We successfully completed the analysis without any problems
Results review and Complete Report	Finished review and report	None

Table 5: Management of the project

8 References

References

- [1] P. E. Clegg, P. A. R. Ade, C. Armand, J. P. Baluteau, M. J. Barlow, M. A. Buckley, J. C. Berges, M. Burgdorf, E. Caux, C. Ceccarelli, R. Cerulli, S. E. Church, F. Cotin, P. Cox, P. Cruvellier, J. L. Culhane, G. R. Davis, A. di Giorgio, B. R. Diplock, D. L. Drummond, R. J. Emery, J. D. Ewart, J. Fischer, I. Furniss, W. M. Glencross, M. A. Greenhouse, M. J. Griffin, C. Gry, A. S. Harwood, A. S. Hazell, M. Joubert, K. J. King, T. Lim, R. Liseau, J. A. Long, D. Lorenzetti, S. Molinari, A. G. Murray, D. A. Naylor, B. Nisini, K. Norman, A. Omont, R. Orfei, T. J. Patrick, D. Pequignot, D. Pouliquen, M. C. Price, Nguyen-Q-Rieu, A. J. Rogers, F. D. Robinson, M. Saisse, P. Saraceno, G. Serra, S. D. Sidher, A. F. Smith, H. A. Smith, L. Spinoglio, B. M. Swinyard, D. Texier, W. A. Towlson, N. R. Trams, S. J. Unger, and G. J. White. The ISO Long-Wavelength Spectrometer. , 315:L38–L42, November 1996.
- [2] Bruce T. Draine. *Physics of the Interstellar and Intergalactic Medium*. 2011.
- [3] V. Escalante, A. Sternberg, and A. Dalgarno. Near-infrared emission of neutral carbon from photon-dominated regions. , 375:630, July 1991.
- [4] Paul F. Goldsmith and William D. Langer. Population diagram analysis of molecular line emission. *The Astrophysical Journal*, 517(1):209, may 1999.
- [5] Janik Karoly, Archana Soam, B. G. Andersson, Simon Coudé, Pierre Bastien, John E. Vaillancourt, and Chang Won Lee. Revisiting the Magnetic Field of the L183 Starless Core. , 900(2):181, September 2020.
- [6] Michael J. Kaufman, Mark. G. Wolfire, and David J. Hollenbach. [Si II], [Fe II], [C II], and H₂ Emission from Massive Star-forming Regions. , 644(1):283–299, June 2006.
- [7] M. F. Kessler, J. A. Steinz, M. E. Anderegg, J. Clavel, G. Drechsel, P. Estaria, J. Faelker, J. R. Riedinger, A. Robson, B. G. Taylor, and S. Ximénez de Ferrán. The Infrared Space Observatory (ISO) mission. , 315(2):L27–L31, November 1996.
- [8] Jeffrey G. Mangum and Yancy L. Shirley. How to calculate molecular column density. *Publications of the Astronomical Society of the Pacific*, 127(949):266–298, mar 2015.
- [9] Andrea Mehner, Kris Davidson, Gary J. Ferland, and Roberta M. Humphreys. High-excitation emission lines near eta carinae, and its likely companion star*. *The Astrophysical Journal*, 710(1):729, jan 2010.
- [10] Dimitri Mihalas. *Stellar atmospheres*. 1978.
- [11] TE Oberst, SC Parshley, T Nikola, GJ Stacey, A Löhr, AP Lane, AA Stark, and J Kamenetzky. A 205 μm [n ii] map of the carina nebula. *The Astrophysical Journal*, 739(2):100, 2011.

- [12] Jaime E. Pineda, Paola Caselli, and Alyssa A. Goodman. CO isotopologues in the perseus molecular cloud complex: the α -factor and regional variations. *The Astrophysical Journal*, 679(1):481–496, may 2008.
- [13] M. W. Pound and M. G. Wolfire. The Photo Dissociation Region Toolbox. In R. W. Argyle, P. S. Bunclark, and J. R. Lewis, editors, *Astronomical Data Analysis Software and Systems XVII*, volume 394 of *Astronomical Society of the Pacific Conference Series*, page 654, August 2008.
- [14] M. W. Pound and M. G. Wolfire. PDRT: Photo Dissociation Region Toolbox, February 2011.
- [15] Roueff, Antoine, Gerin, Maryvonne, Gratier, Pierre, Levrier, François, Pety, Jérôme, Gaudel, Mathilde, Goicoechea, Javier R., Orkisz, Jan H., de Souza Magalhaes, Victor, Vono, Maxime, Bardeau, Sébastien, Bron, Emeric, Chanussot, Jocelyn, Chainais, Pierre, Guzman, Viviana V., Hughes, Annie, Kainulainen, Jouni, Languignon, David, Le Bourlot, Jacques, Le Petit, Franck, Liszt, Harvey S., Marchal, Antoine, Miville-Deschênes, Marc-Antoine, Peretto, Nicolas, Roueff, Evelyne, and Sievers, Albrecht. C18o, 13co, and 12co abundances and excitation temperatures in the orion b molecular cloud - analysis of the achievable precision in modeling spectral lines within the approximation of the local thermodynamic equilibrium. *A&A*, 645:A26, 2021.
- [16] F. L. Schöier, F. F. S. van der Tak, E. F. van Dishoeck, and J. H. Black. An atomic and molecular database for analysis of submillimetre line observations. , 432(1):369–379, March 2005.
- [17] Young Min Seo, C. Darren Dowell, Paul F. Goldsmith, Jorge L. Pineda, and Liton Majumdar. Probing polarization and the role of magnetic fields in cloud destruction in the keyhole nebula. *The Astrophysical Journal*, 917(2):57, aug 2021.
- [18] Raphael Skolidis and Konstantinos Tassis. High-accuracy estimation of magnetic field strength in the interstellar medium from dust polarization. , 647:A186, March 2021.
- [19] Lyman Spitzer. *Physical processes in the interstellar medium*. 1978.
- [20] F. F. S. van der Tak, J. H. Black, F. L. Schöier, D. J. Jansen, and E. F. van Dishoeck. A computer program for fast non-LTE analysis of interstellar line spectra. With diagnostic plots to interpret observed line intensity ratios. , 468(2):627–635, June 2007.
- [21] Ewine F. van Dishoeck, Bastiaan Jonkhed, and Marc C. van Hemert. Photoprocesses in protoplanetary disks. *Faraday Discuss.*, 133:231–243, 2006.
- [22] Ramonda Visser, E. Dishoeck, and J. Black. The photodissociation and chemistry of co isotopologues: Applications to interstellar clouds and circumstellar disks. *Astronomy and Astrophysics*, 503, 06 2009.

9 Appendix

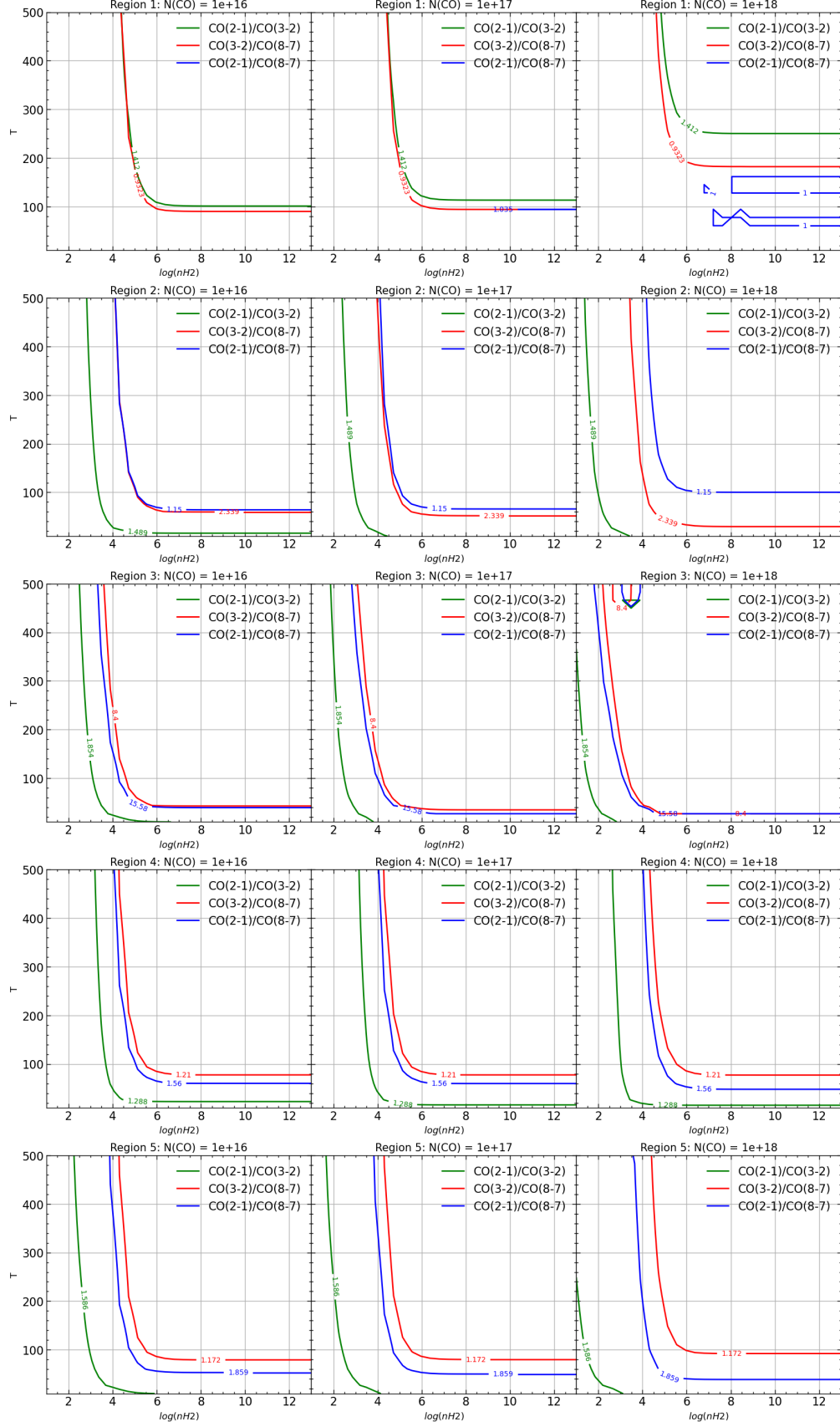


Figure 2: Physical constraint using RADEX of Region 1-5

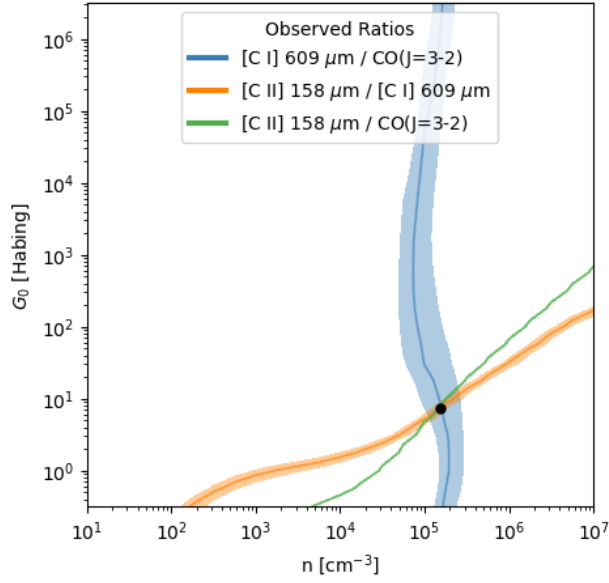


Figure 3: Overlay plots show the observed intensity ratios in the G_0 and n_H grids of the PDR Toolbox. The shaded area represents the observational error.

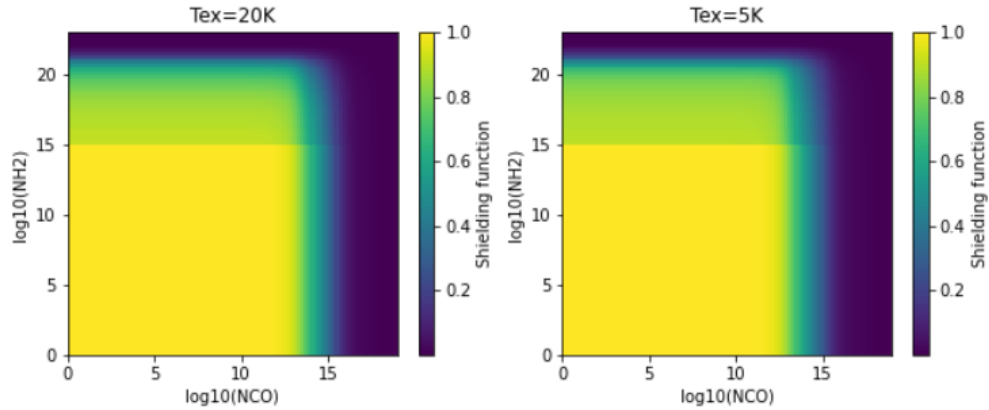
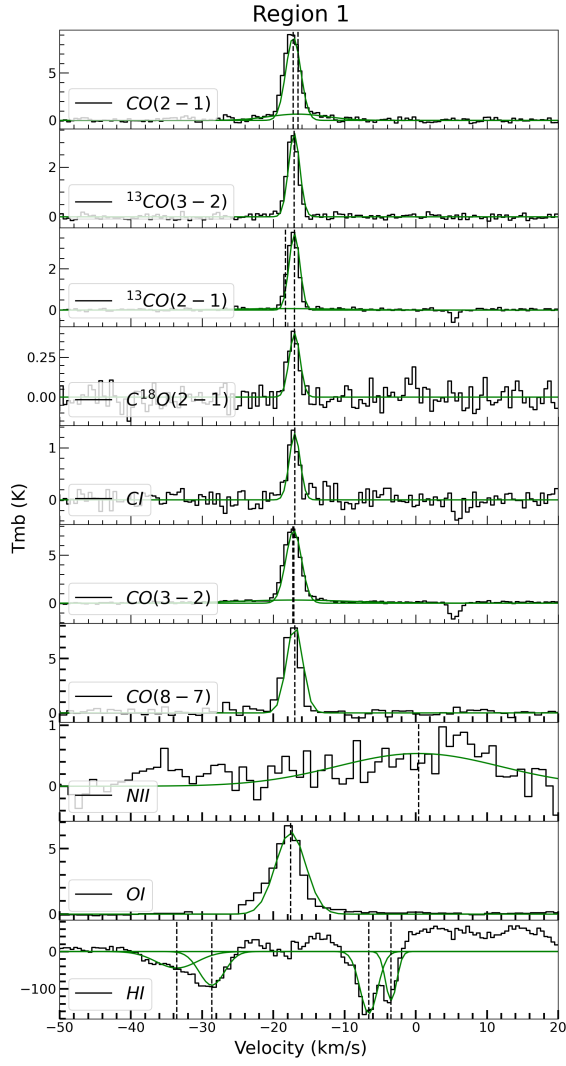
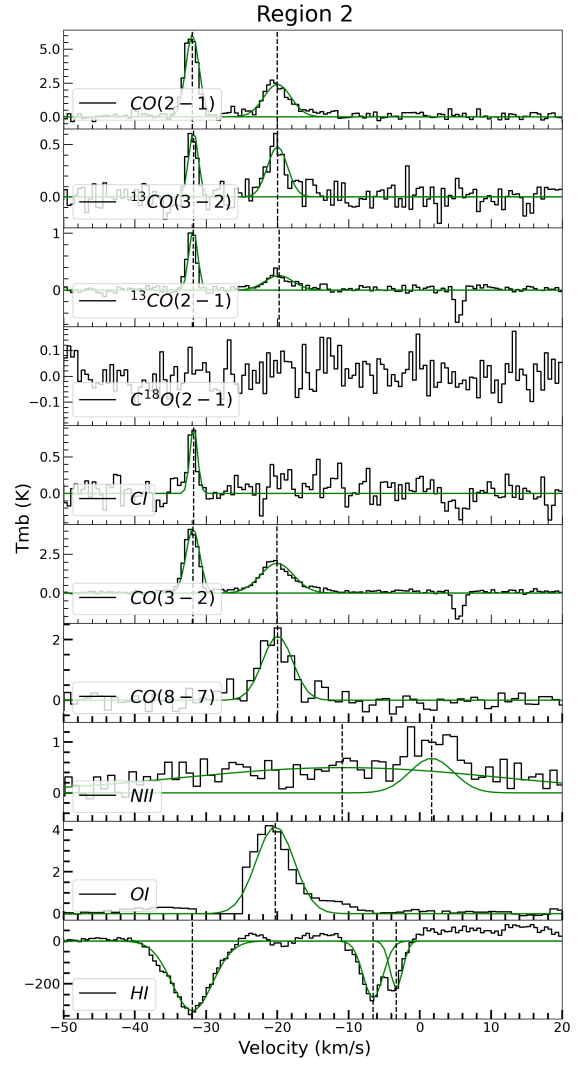


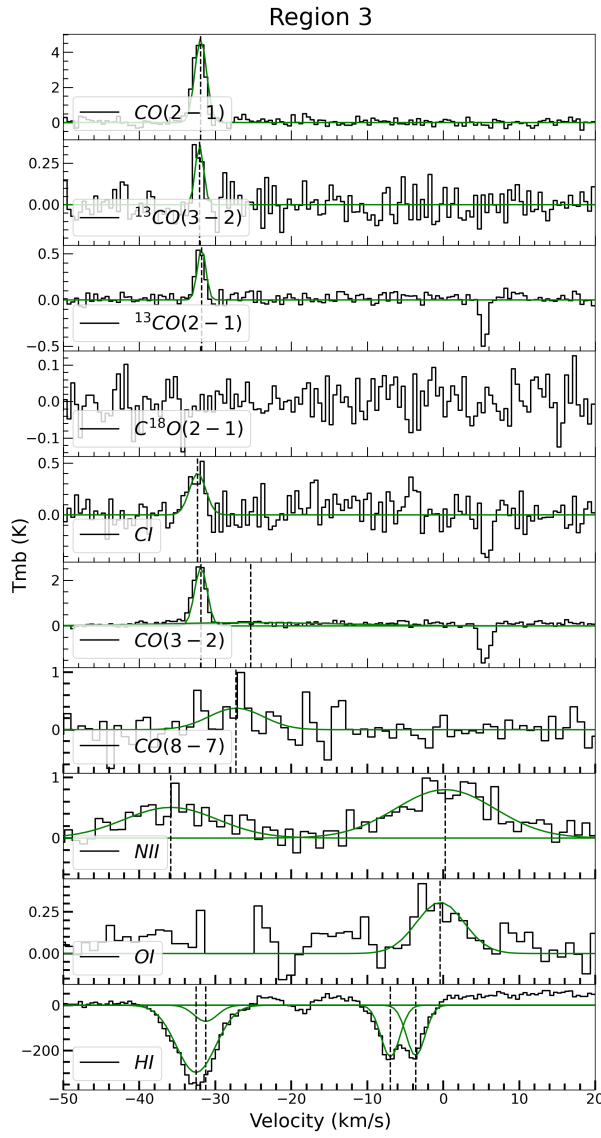
Figure 4: Shielding function by gas and ^{12}CO at $T_{ex} = 20K$ and $T_{ex} = 5K$



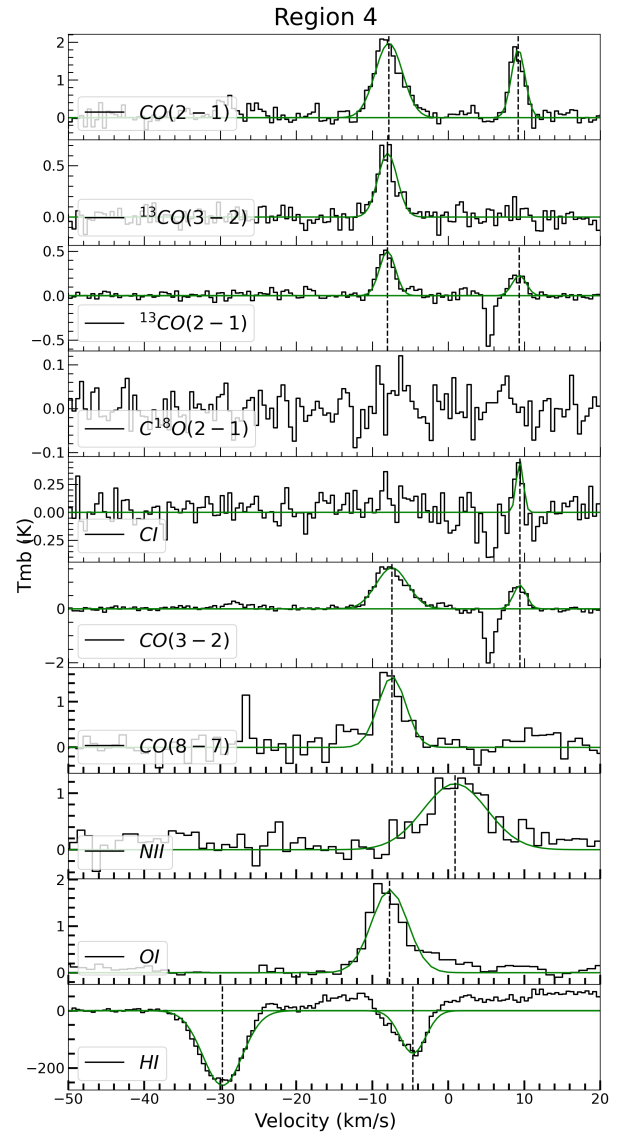
(a) Region 1



(b) Region 2



(c) Region 3



(d) Region 4

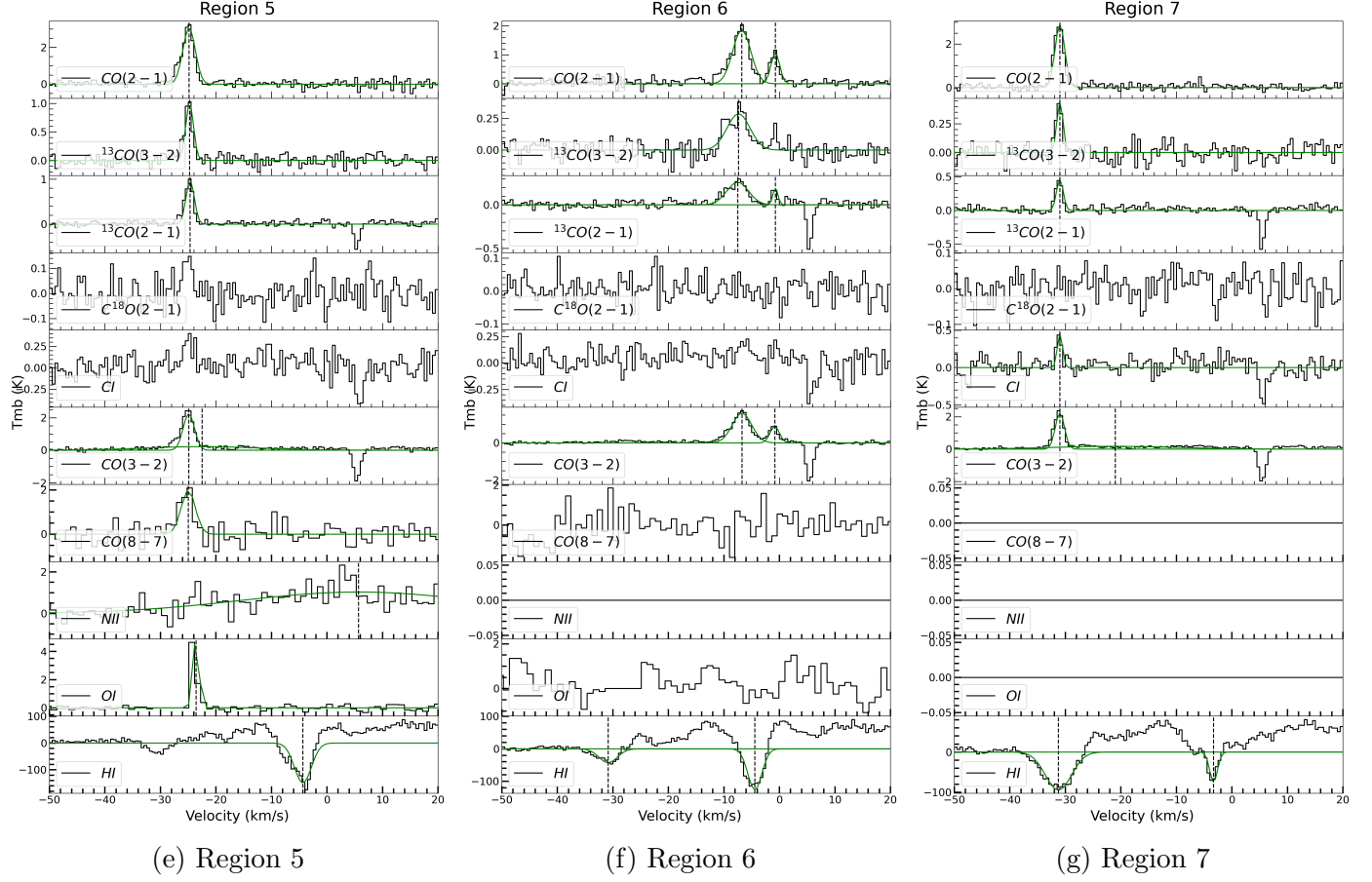


Figure 5: Representative spectra of $^{12}CO(2-1)$, $^{13}CO(3-2)$, $^{13}CO(2-1)$, $C^{18}O(2-1)$, $[C\ I]$ 609 μ m, $^{12}CO(3-2)$, $^{12}CO(8-7)$, $[N\ II]$ 205 μ m, $[O\ I]$ 63 μ m and 21 cm H towards the 7 regions.

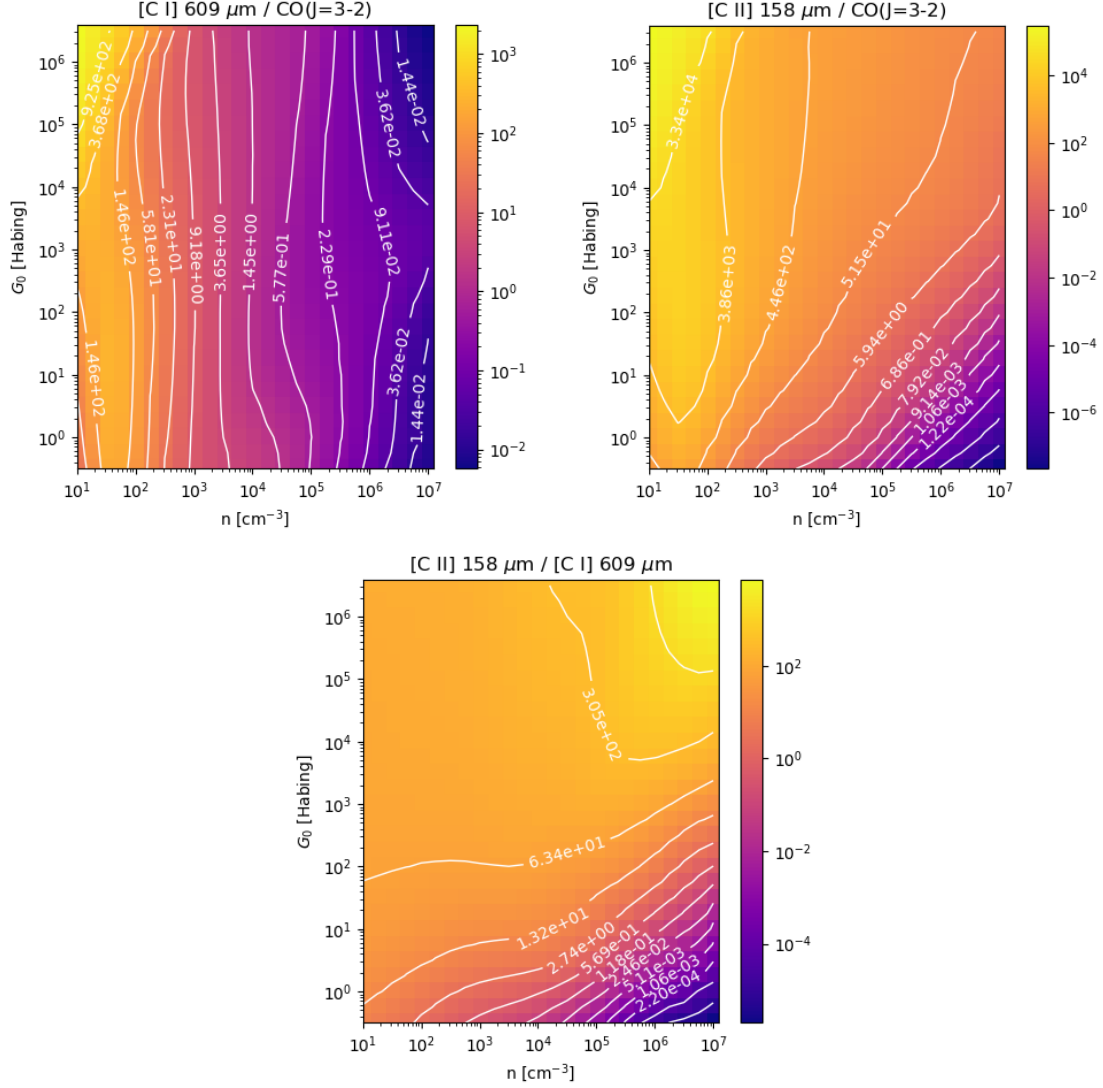


Figure 6: The WK2006 model for the ratio of the [C I] 609 μm and $^{12}\text{CO}(3-2)$ (top left), [C II] 158 $\mu\text{m}/^{12}\text{CO}(3-2)$ (top right) and [C II] 158 $\mu\text{m}/[\text{C I}]$ 609 μm (bottom), computed as a function of hydrogen nucleus density n_H and FUV field G_0 .

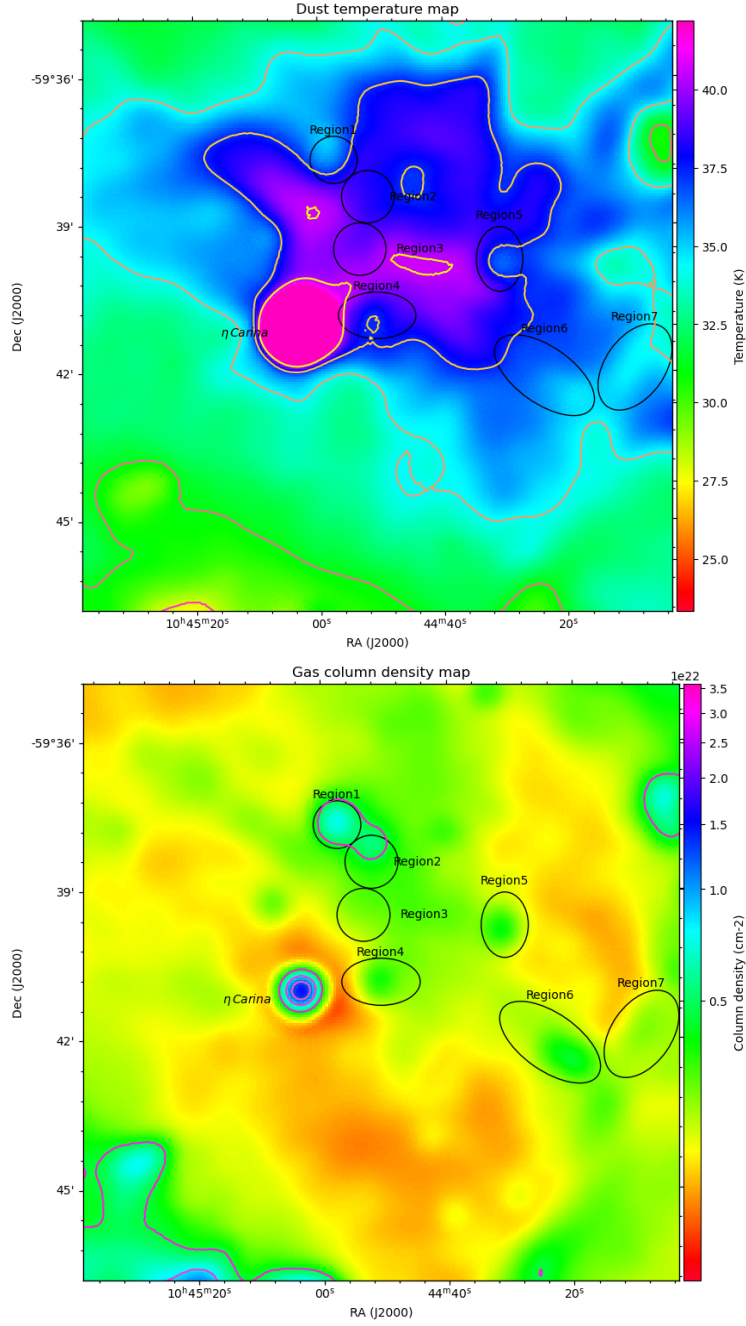


Figure 7: The top panel shows the fitted dust temperature T_d map, and the bottom panel shows the corresponding column density N_{H_2} map. Each map is smoothed to the 35.2 beam size of the Herschel 500 μ m observations